IIETA International Information and Engineering Technology Association
Advancing the World of Information and Engineering

Traitement du Signal
Vol. 43, No. 2, April, 2026, pp. 667-673
Journal homepage: http://iieta.org/journals/ts

Deep Learning Framework for Distinguishing Fresh and Old Osteoporotic Vertebral Compression Fractures on Lateral Spine Radiographs

Yuqing Guo, Helong Wang, Lina Sun*

Harbin Medical University, Harbin 150081, China

Corresponding Author Email: sunlina@hrbmu.edu.cn

https://doi.org/10.18280/ts.430209

Received: 12 August 2025
Revised: 19 January 2026
Accepted: 12 February 2026
Available online: 30 April 2026

Keywords:
deep learning, fresh osteoporosis vertebral fractures, spine lateral radiography

ABSTRACT

Osteoporotic vertebral compression fractures (OVCFs) are the most common osteoporotic fractures in the elderly. Growing evidence indicates that Artificial Intelligence (AI) approaches can match physician-level performance in identifying osteoporotic vertebral fractures across multiple imaging modalities, including X-ray, CT, and magnetic resonance imaging (MRI). Nonetheless, automated identification of acute OVCFs on plain lateral spine radiographs remains largely unexplored, despite its critical implications for clinical decision-making. In this paper, a Deep Convolutional Neural Network (DCNN) was pretrained on ImageNet and subsequently fine-tuned using 720 vertebral image patches extracted from lateral spine radiographs of 405 OVCF patients. The radiographs are obtained from the Harbin Medical University Cancer Hospital. To evaluate the classification performance of the proposed model, the metrics of accuracy, sensitivity, specificity, and area under the receiver operating characteristic curve (AUC) are estimated on the validation set, achieving an accuracy of 75.13 ± 2.62%, a specificity of 76.81 ± 5.59%, a sensitivity of 75.50 ± 3.31%, and an AUC of 0.796 ± 0.028. In addition, the model's diagnostic performance surpassed that of attending clinicians, suggesting its considerable promise as a decision-support tool in the clinical management of acute OVCFs.

1. INTRODUCTION

Osteoporotic vertebral compression fractures (OVCFs) typically arise from low-energy trauma or even without any precipitating event, and represent one of the most burdensome skeletal complications worldwide [1, 2]. OVCFs are most common in the thoracolumbar segment T11-L5, and commonly in the elderly population. Among them, the wedge compression fracture is the most common (51%), frequently giving rise to chronic low back pain, progressive kyphotic deformity, and diminished pulmonary capacity, ultimately contributing to reduced quality of life and elevated mortality [3]. Currently, percutaneous kyphoplasty or vertebroplasty is the most mainstream surgical treatment for fresh OVCF [4, 5], as it can restore vertebral body height and mechanical strength, limit further collapse, and provide meaningful pain relief. Allowing patients to resume daily activities sooner with less surgical trauma and a shorter hospitalization [6]. However, these procedures are only indicated for acute fractures; chronic OVCFs are considered a relative contraindication [7]. Consequently, reliably distinguishing acute from chronic fractures prior to surgical planning is of paramount clinical importance.

Imaging serves as the primary modality for OVCF evaluation. On plain radiographs, acute fractures may be suggested by discrete cortical disruptions and visible fracture lines, whereas vertebral wedging, endplate sclerosis, and peripheral bone overgrowth are indicative of chronic injury. However, clear fracture lines are rarely seen in fresh OVCFs, which are caused by lower energy trauma or without trauma, many present as occult fractures without any discernible morphological difference from adjacent intact vertebrae on X-ray [8], or there is a compression of the vertebral body, but no clear fracture line can be seen on the cortical bone. Differentiating acute from chronic fractures on plain films is inherently challenging, particularly for less experienced clinicians. Magnetic resonance imaging (MRI) can more accurately assess the presence or absence of spinal canal compression and the freshness of fractures, and it is also the main examination to distinguish fresh and old vertebral compression fractures at present [9]. Bone marrow edema accompanying acute intravertebral injury manifests as hyperintensity on T2-weighted and STIR sequences, with corresponding T1 hypointensity. However, MRI is expensive, time-consuming, and unavailable in many primary care settings, and is poorly tolerated by a subset of OVCF patients. There is therefore a pressing clinical need for an accurate, rapid, and cost-effective diagnostic approach to differentiate acute from chronic thoracolumbar compression fractures.

These diagnostic challenges have driven growing interest in automated computational solutions. Deep learning (DL) has emerged as a transformative technology in medical imaging, with its applications expanding rapidly [10]. As far as OVCFs are concerned, several DL-based systems have been reported. For example, Chen et al. [11] proposed a framework integrating 3D V-Net segmentation with ResNet18-based

classification, achieving Area Under the Receiver Operating Characteristic Curve (AUC) values of 0.96 on internal validation and 0.87 on prospective testing for fresh/old OVCF discrimination on thoracolumbar CT, demonstrating superiority over human readers. Yabu et al. [12] described an MRI-based DL approach for detecting acute osteoporotic vertebral fractures. Li et al. [13] examined DL-assisted differentiation of benign from malignant vertebral fractures using CT imaging. Chen et al. [14] developed a deep-learning model built by ResNet 50 for identifying fresh vertebral compression fractures on digital radiography and achieved an accuracy of 74%. However, that model was trained on a mixed dataset of anteroposterior and lateral projections, whereas in routine practice, spine surgeons and radiologists almost exclusively rely on the lateral view [15, 16]. To our knowledge, no prior study has specifically applied DL to classify fresh versus old OVCFs using lateral spine radiographs alone.

The present work introduces a DL-based classification model for identifying acute OVCFs on lateral spine radiographs, using MRI findings combined with clinical records as the reference standard. The primary aim is to quantitatively evaluate the automated classifier's performance and to benchmark it against orthopaedic surgeons and radiologists.

2. MATERIALS AND METHODS

2.1 Materials

2.1.1 Patient population

This retrospective study received approval from the institutional review board and ethics committee of Harbin Medical University Cancer Hospital; informed consent was waived, and all data were de-identified prior to analysis. For the retrospective study, the images and the data of 557 patients from October 2016 to January 2022 were collected. Patients were eligible if they (1) were aged 60 years or older and (2) had sustained OVCFs through low-energy mechanisms or without a clearly identifiable trauma history. Cases were excluded if there was (1) a known history of vertebral metastasis or haematological malignancy, (2) unavailable or technically inadequate thoracolumbar radiographs, (3) unavailable MRI, or (4) an interval exceeding one week between radiography and MRI acquisition. Finally, 405 patients were included in the study (see Figure 1).

2.1.2 Standard for diagnosis

Expert interpretation of MRI in conjunction with a thorough review of the patient's medical history is widely accepted as the reference standard for distinguishing acute from chronic OVCFs. Acute OVCFs were characterised on MRI by elevated signal on T2-weighted and STIR sequences alongside reduced signal on T1-weighted images. And the medical records showed vertical percussed pain at the corresponding vertebral segment contributed by the lower energy trauma or without a history of obvious trauma, which was used to exclude misdiagnosis caused by possible image artifacts on MRI. For the old OVCF, radiographs showed vertebral compression at the corresponding level, while MRI showed no obvious above signals except the vertebral compression, and there was no significant pain at the corresponding vertebral segment. The labelled lateral radiographs assigned by human readers served as ground-truth annotations for model training, testing, and validation.

2.2 Methods

The overall workflow of the proposed DL framework is summarised in Figure 2, encompassing six sequential stages from image annotation to final model selection.

Figure 2 illustrates the overall workflow of the proposed DL framework. The pipeline begins with manual annotation of the region of interest (ROI) on lateral spine radiographs by two experienced spine surgeons (a), followed by cropping of each annotated vertebral segment into an individual image patch (b). Histogram equalisation was then applied to enhance local contrast and recover subtle structural detail (c), after which each patch was assigned a fresh or old label based on MRI reference standards (d). Five CNN architectures—AlexNet, VGG16, GoogLeNet, ResNet50, and ResNet101—were subsequently trained and evaluated under identical preprocessing conditions (e), and ResNet101 was ultimately selected as the final classification model on the basis of its superior performance across all reported metrics (f). The individual steps of this pipeline are described in detail in the following subsections.

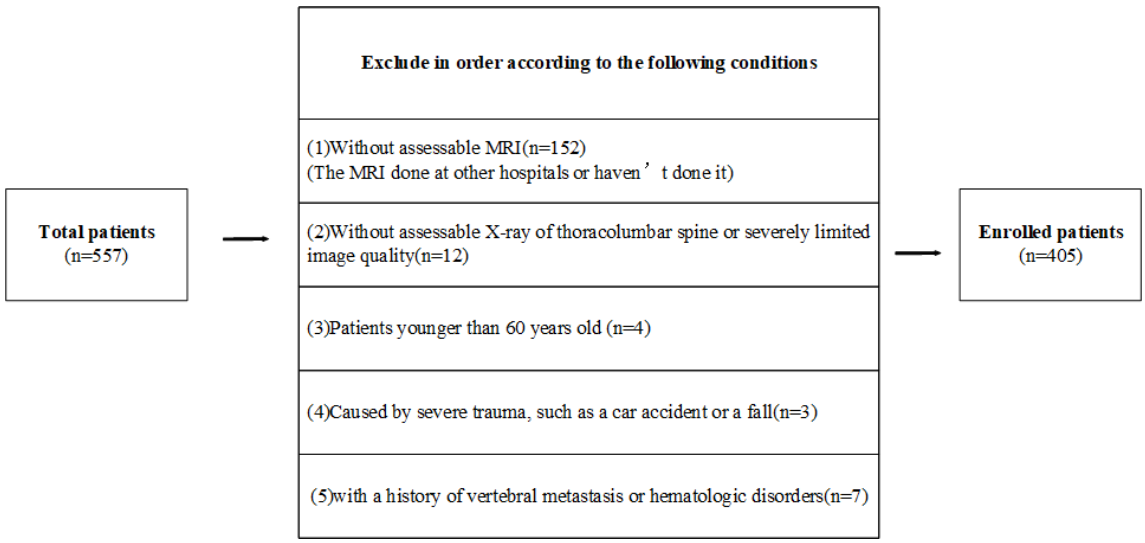

Figure 1. Flow chart of study exclusion and inclusion

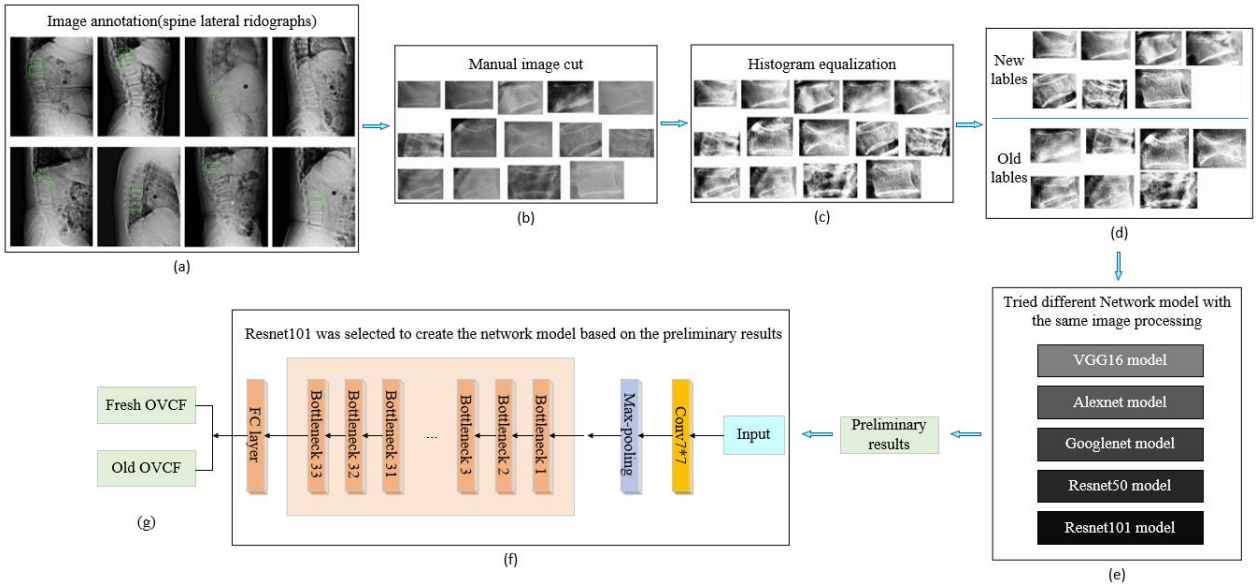

Figure 2. General flow-chart

(a) Image annotation for the spine lateral radiographs. (b) Manually cut the annotated area. (c) Histogram equalization is carried out on the image. (d) Divide the image into new and old labels. (e)Tried different network models with the same image processing. (f) ResNet50 was selected to create the network model based on the preliminary results

2.2.1 Image annotation and dataset establishment

Image labelling was performed independently by two experienced spine surgeons (GWS and GZ, with 27 and 11 years of clinical experience, respectively) in accordance with the diagnostic criteria described above. Discordant cases were resolved through joint review of the corresponding MRI scans and medical records until consensus was reached, thereby identifying the true ROI. Then, they used Photoshop2019 (Microsoft Co.) to cut the ROI directly to obtain the corresponding image format, with the image boundary within the target range of 1–10 mm, and labeled as new or old.

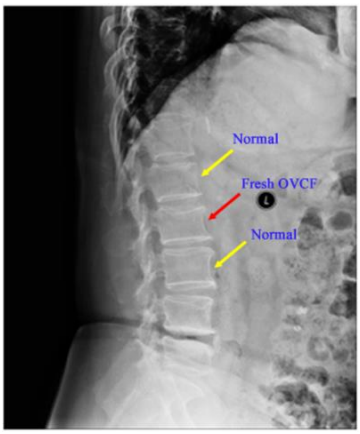

Figure 3. Comparison of vertebral height between the acute fracture segment and the adjacent vertebral body showed no significant difference

However, in the segments of confirmed fresh OVCFs, there are a small number (11 slices) without significant vertebral compression (see Figure 3), which appear to be similar to the normal vertebral body in vertebral height, and it is more likely to be considered a normal rather than a compression fracture after healing, while we can only identify old OVCFs with compression of the vertebral body without obvious specific manifestations on MRI or the medical records, and fresh fracture segments mentioned above after healing are more likely to be diagnosed as normal instead of old fracture. To improve model robustness, nine anatomically normal vertebral segments were intentionally assigned old labels. And there was at least one slice taken from each patient, even some fresh and old slices were obtained from the different vertebral segments of the same patient. Finally, 720 slices of images were obtained from plain lateral radiographs of 405 patients with OVCF. Among them, 364 slices were labeled as fresh and 356 slices as old. The dataset details are shown in Table 1. Two-sample t-test (IBM, SPSS, version26.0) was used to analyze the distribution of fresh and old vertebral fractures at different levels, and 95% confidence intervals (CIs) were obtained, which showed no significant difference.

Table 1. Demographic data of included patients (the number of normal segments added for the corresponding vertebral segment is shown in parentheses)

Parameter	Value	
Age	75 ± 14	
The number of females	290	
The number of males	115	
Fracture segment	Fresh OVCF	Old OVCF
T5	3	3
T6	13	12
T7	11	17
T8	22	24(1)
T9	17	18
T10	16	13
T11	33	34(1)
T12	71	61(2)
L1	75	57(3)
L2	45	41(2)
L3	29	30(1)
L4	21	31(1)
L5	8	15
p value	0.939 > 0.05	
Total	364	356

2.2.2 Image preprocessing

Because pixel intensity values in radiographic images tend to cluster within a narrow dynamic range, histogram

equalisation [17] was applied during preprocessing to amplify local contrast and recover subtle structural detail. And images were normalized by rescaling pixel values to [-1,1] and were resized to 224 × 224 × 3. The training subset was augmented through random left–right and top–bottom flipping to reduce overfitting and improve tolerance to imaging variability.

2.2.3 Deep learning model comparison and selection

We used the concept of transfer learning [18] to train the Artificial Intelligence (AI) model, which contains VGG16 [19], Alexnet [20], Googlenet [21], ResNet50 [13], and ResNet101 [22]. The weights obtained on the pretrained ImageNet data were used as the initial weights for our Deep Convolutional Neural Network (DCNN) model training. All five architectures were trained under identical preprocessing conditions to allow fair comparison, and ResNet101 was ultimately selected based on its superior overall performance (Figure 2(f)).

2.2.4 Selected model framework

The ResNet101 architecture contained one 7 × 7 convolutional layer, one max-pooling layer, and 33 Bottleneck modules that are divided into four layers (the number of modules in each layer is 3, 4, 23, and 3, respectively). Each Bottleneck module contained three convolutional layers, three batch normalization layers, and one ReLU activation function layer. The output of the last block was connected to a fully connected layer with a Linear function to make the prediction, by giving a fresh OVCF probability. Residual connections facilitate gradient propagation during training and mitigate the vanishing-gradient problem. The bottleneck structure reduces per-layer computational cost, enabling a substantially deeper architecture without a proportional increase in training time. Therefore, the ResNet101 pretrained network model was applied to build our network model framework.

3. EXPERIMENTS

3.1 Network training details

ResNet was initialised with weights from ImageNet via transfer learning to enhance downstream classification performance. Optimisation used cross-entropy loss [23] with an initial learning rate of 0.001 and momentum of 0.9. Training ran for 100 epochs with a learning rate decay factor of 0.8 applied every 30 epochs. The software to build the DCNN is based on the open-source libraries Python 3.80 and PyTorch, and the training process runs on an Intel Core i7-8750H CPU 4.30GHz and GeForce GTX 1060 GPU.

3.2 Statistical analysis

Model performance was assessed using specificity, sensitivity, precision, accuracy, F1 score (Eqs. (1)–(5)), and AUC, all derived from the confusion matrix elements: true positive (TP), false positive (FP), false negative (FN), and true negative (TN).

$$\text{Specificity} = \frac{\text{TN}}{\text{TN} + \text{FP}} \tag{1}$$

$$\text{Recall} = \text{Sensitivity} = \frac{\text{TP}}{\text{TP} + \text{FN}} \tag{2}$$

$$\text{Precision} = \frac{\text{TP}}{\text{TP} + \text{FP}} \tag{3}$$

$$\text{Accuracy} = \frac{\text{TP} + \text{TN}}{\text{TP} + \text{TN} + \text{FP} + \text{FN}} \tag{4}$$

$$\text{F1 score} = 2 \times \frac{\text{Recall} \times \text{Precision}}{\text{Recall} + \text{Precision}} \tag{5}$$

4. RESULTS AND DISCUSSION

Five CNN architectures were evaluated under uniform conditions—all initialised from ImageNet pre-trained weights and tested on the same held-out dataset—with performance compared across accuracy, precision, recall, F1 score, and AUC. The performance of each CNN is shown in Table 2. ResNet101 outperformed all other architectures across every reported metric, attaining a peak accuracy of 75.13 ± 2.62% and an AUC of 0.800 ± 0.042.

Generalisation was further assessed through five-fold cross-validation of ResNet101 (Table 3); Fold 2 yielded the highest AUC, with the corresponding ROC curves and confusion matrices shown in Figure 4. Furthermore, four orthopedic surgeons and one radiologist (Orthopedic surgeons include GWS, GZ, RB, XZY, 27, 11, 10, and 5, respectively, and one radiologist ZS with 3 years of clinical experience) were separately asked to diagnose 40 images randomly selected from the test dataset without histogram equalization to compare with the results of artificial intelligence, in which the paired t test was adopted (Table 4).

The model substantially outperformed all five clinicians; physician performance was constrained by the absence of adjacent vertebral context in the cropped patches, departing from conventional radiograph reading habits. It did not conform to the doctors' habit of reading radiography in a cut small piece that cannot be compared with the upper and lower vertebral segments, but it provided the target vertebral segments directly, in which only the texture of the vertebral body images needs to be analyzed to distinguish between fresh and old, and no need to compare adjacent segments to see if they were compressed. Three days later, after consulting the model output, clinicians repeated their assessments on the same images, and diagnostic accuracy improved significantly for all readers (Table 5).

Table 2. Comparative results of various neural network models in our test dataset

Model	Accuracy (%)	Precision (%)		Recall (%)		F1-score (%)		AUC
		Fresh	Old	Fresh	Old	Fresh	Old	
AlexNet	69.72 ± 1.55	70.02 ± 4.00	70.12 ± 2.99	68.80 ± 7.63	70.61 ± 7.57	70.65 ± 2.85	70.09 ± 2.70	0.734 ± 0.215
Vgg16	71.26 ± 2.62	71.50 ± 4.43	71.35 ± 0.70	70.50 ± 2.76	71.98 ± 7.8	70.85 ± 1.07	71.51 ± 4.32	0.735 ± 0.036
GoogleNet	71.11 ± 2.27	72.50 ± 3.88	70.51 ± 3.64	67.72 ± 7.56	74.43 ± 6.62	69.72 ± 3.48	72.20 ± 2.54	0.763 ± 0.040
ResNet50	73.60 ± 2.55	75.12 ± 4.08	73.64 ± 6.25	70.79 ± 11.50	76.39 ± 8.36	72.27 ± 4.99	74.45 ± 2.17	0.762 ± 0.035
ResNet101	75.69 ± 2.08	76.81 ± 5.59	75.50 ± 3.31	73.90 ± 6.71	77.45 ± 8.03	74.98 ± 2.27	76.18 ± 3.00	0.796 ± 0.028

Table 3. Comparison of performances of the five-fold cross-validation of ResNet101

5-fold	Accuracy (%)	Precision (%)		Recall (%)		F1-Score (%)		AUC
		New	Old	New	Old	New	Old	
Fold 1	77.24	85.45	72.22	65.28	89.04	74.02	79.75	0.808
Fold 2	77.78	79.10	76.62	74.65	80.82	76.81	78.67	0.843
Fold 3	72.92	74.24	71.79	69.01	76.71	71.53	74.17	0.760
Fold 4	76.39	74.03	79.10	80.28	72.60	77.03	75.71	0.791
Fold 5	74.13	71.25	77.78	80.28	68.06	75.50	72.59	0.780
Average	75.69 ± 2.08	76.81 ± 5.59	75.50 ± 3.31	73.90 ± 6.71	77.45 ± 8.03	74.98 ± 2.27	76.18 ± 3.00	0.796 ± 0.028
p value	-	0.664 > 0.05		0.470 > 0.05		0.496 > 0.05		-

Table 4. Comparison of network model performance with physicians' diagnoses

Objects	Accuracy (%)	Specificity (%)	Sensitivity (%)
Doctor 1 (GWS)	45.00	45.00	45.00
Doctor 2 (GZ)	55	57.14	53.85
Doctor 3 (RB)	52.5	52.94	45
Doctor 4 (XZY)	50	50	50
Doctor 5 (ZS)	55	56.25	54.17
Average	51.50 ± 4.18	52.27 ± 4.95	49.60 ± 4.51
ResNet101	75.69 ± 2.08	76.81 ± 5.59	75.50 ± 3.31
p value	0.001	0.004	< 0.001

Note: Significant differences by paired t-test are reported in the last row.

Table 5. Comparison of physicians' results with and without Artificial Intelligence (AI) assistance

Objects	Accuracy (%)	Specificity (%)	Sensitivity (%)
Doctor 1 (GWS)	62.50	60.87	64.71
Doctor 2 (GZ)	72.50	76.47	69.57
Doctor 3 (RB)	70.00	72.22	68.18
Doctor 4 (XZY)	65.00	68.75	62.50
Doctor 5 (ZS)	67.50	68.42	66.67
Average result with AI	67.50 ± 3.95	69.33 ± 5.72	66.33 ± 2.80
Without AI assistance	51.50 ± 4.18	52.27 ± 4.95	49.60 ± 4.51
p value	< 0.001	< 0.001	0.001 < 0.05

Note: Significant differences by paired t-test are reported in the last row.

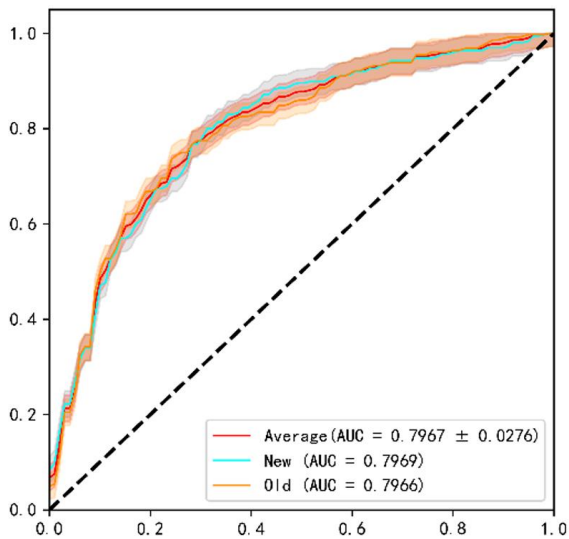

Figure 4. The receiver operating characteristic (ROC) curves of the five-fold cross-validation of Resnet101

5. CONCLUSION

The proposed CNN-based model demonstrated the capacity to automatically differentiate fresh from old OVCFs on lateral spine radiographs, with diagnostic accuracy exceeding that of experienced spine surgeons.

Kyphoplasty and vertebroplasty remain the primary surgical options for OVCF [24], and prompt minimally invasive intervention is generally regarded as the preferred strategy based on clinical evidence [25]. In chronic fractures, the vertebral body undergoes sclerotic consolidation, impeding cement infiltration, increasing the risk of cement extravasation, and precluding meaningful height restoration. Accordingly, old OVCFs are a relative contraindication to minimally invasive cement augmentation. Prompt identification of acute fractures and confident exclusion of chronic ones therefore carries substantial clinical relevance, facilitating aetiological determination and excluding non-vertebral sources of thoracic or lumbar pain even when surgery is deferred.

A practical decision-support tool could be developed on this basis, enabling clinicians to submit a manually identified vertebral segment for automated classification, with the final interpretation informed by integrated clinical assessment. Nonetheless, there are limitations to the current study. First, the single-centre dataset is relatively small, contributing to variability across cross-validation folds. The native diaphragm is the major obstacle to the better performance of our AI model. If the data volume is large enough, consider dividing the data into three categories: subdiaphragmatic, diaphragmatic, and subdiaphragmatic, then classifying fresh and old vertebral compression fractures separately. Second, the model does not account for fractures attributable to haematological disorders, primary bone tumours, or metastatic disease; clinicians must remain alert to these alternative

aetiologies to avoid missed diagnoses.

REFERENCES

[1] Santiago, F.R., Muñoz, P.T., Sánchez, E.M., Paniza, M.R., Martínez, A.M., Abela, A.L.P. (2016). Classifying thoracolumbar fractures: Role of quantitative imaging. Quantitative Imaging in Medicine and Surgery, 6(6): 772-784. https://doi.org/10.21037/qims.2016.12.04

[2] Bliuc, D., Nguyen, N.D., Milch, V.E., Nguyen, T.V., Eisman, J.A., Center, J.R. (2009). Mortality risk associated with low-trauma osteoporotic fracture and subsequent fracture in men and women. JAMA, 301(5): 513-521. https://doi.org/10.1001/jama.2009.50

[3] Lieberman, I.H., Dudeney, S., Reinhardt, M.K., Bell, G. (2001). Initial outcome and efficacy of "kyphoplasty" in the treatment of painful osteoporotic vertebral compression fractures. Spine, 26(14): 1631-1637.

[4] Masoudi, M.S., Haghnegahdar, A., Ghaffarpasand, F., Ilami, G. (2017). Functional recovery following early kyphoplasty versus conservative management in stable thoracuolumbar fractures in parachute jumpers: A randomized clinical trial. Clinical Spine Surgery, 30(8): E1066-E1073. https://doi.org/10.1097/BSD.0000000000000546

[5] Klazen, C.A., Lohle, P.N., De Vries, J., Jansen, F.H., et al. (2010). Vertebroplasty versus conservative treatment in acute osteoporotic vertebral compression fractures (Vertos II): An open-label randomised trial. The Lancet, 376(9746): 1085-1092. https://doi.org/10.1016/S0140-6736(10)60954-3

[6] Phillips, F.M. (2003). Minimally invasive treatments of osteoporotic vertebral compression fractures. Spine, 28(15S): S45-S53. https://doi.org/10.1097/01.BRS.0000076898.37566.32

[7] Shengzhong, M., Dongjin, W., Shiqing, W., Yang, S., Peng, R., Wanli, M., Chunzheng, G. (2012). Modification of percutaneous vertebroplasty for painful old osteoporotic vertebral compression fracture in the elderly: Preliminary report. Injury, 43(4): 486-489. https://doi.org/10.1016/j.injury.2011.12.021

[8] Terakado, A., Orita, S., Inage, K., Kubota, G., et al. (2017). A clinical prospective observational cohort study on the prevalence and primary diagnostic accuracy of occult vertebral fractures in aged women with acute lower back pain using magnetic resonance imaging. Pain Research and Management, 2017(1): 9265259. https://doi.org/10.1155/2017/9265259

[9] Jin, Z.G., Shen, S.M., Gao, J.X., Wang, X.P., Liu, H.M., Lu, W.X., Shen, K. (2011). Identification of fresh and old vertebral compression fractures by MRI. Fa Yi Xue Za Zhi, 27(4): 274-276.

[10] González, G., Ash, S.Y., Vegas-Sánchez-Ferrero, G., Onieva Onieva, J., et al. (2018). Disease staging and prognosis in smokers using deep learning in chest computed tomography. American Journal of Respiratory and Critical Care Medicine, 197(2): 193-203. https://doi.org/10.1164/rccm.201705-0860OC

[11] Chen, J., Liu, S., Li, Y., Zhang, Z., et al. (2025). Deep learning model for automated detection of fresh and old vertebral fractures on thoracolumbar CT. European Spine Journal, 34(3): 1177-1186. https://doi.org/10.1007/s00586-024-08623-w

[12] Yabu, A., Hoshino, M., Tabuchi, H., Takahashi, S., et al. (2021). Using artificial intelligence to diagnose fresh osteoporotic vertebral fractures on magnetic resonance images. The Spine Journal, 21(10): 1652-1658. https://doi.org/10.1016/j.spinee.2021.03.006

[13] Li, Y., Zhang, Y., Zhang, E., Chen, Y., et al. (2021). Differential diagnosis of benign and malignant vertebral fracture on CT using deep learning. European radiology, 31(12): 9612-9619. https://doi.org/10.1007/s00330-021-08014-5

[14] Chen, W., Liu, X., Li, K., Luo, Y., et al. (2022). A deep-learning model for identifying fresh vertebral compression fractures on digital radiography. European Radiology, 32(3): 1496-1505. https://doi.org/10.1007/s00330-021-08247-4

[15] Nevitt, M.C., Ettinger, B., Black, D.M., Stone, K., et al. (1998). The association of radiographically detected vertebral fractures with back pain and function: A prospective study. Annals of Internal Medicine, 128(10): 793-800. https://doi.org/10.7326/0003-4819-128-10-199805150-00001

[16] Yamauchi, K., Adachi, A., Kameyama, M., Murakami, M., Sato, Y., Kato, C., Kato, T. (2020). A risk factor associated with subsequent new vertebral compression fracture after conservative therapy for patients with vertebral compression fracture: A retrospective observational study. Archives of Osteoporosis, 15(1): 9. https://doi.org/10.1007/s11657-019-0679-x

[17] Wang, C., Ye, Z. (2005). Brightness preserving histogram equalization with maximum entropy: A variational perspective. IEEE Transactions on Consumer Electronics, 51(4): 1326-1334. https://doi.org/10.1109/TCE.2005.1561863

[18] Pan, S.J., Yang, Q. (2009). A survey on transfer learning. IEEE Transactions on Knowledge and Data Engineering, 22(10): 1345-1359. https://doi.org/10.1109/TKDE.2009.191

[19] Zhao, D., Zhu, D., Lu, J., Luo, Y., Zhang, G. (2018). Synthetic medical images using F&BGAN for improved lung nodules classification by multi-scale VGG16. Symmetry, 10(10): 519. https://doi.org/10.3390/sym10100519

[20] Lu, S., Lu, Z., Zhang, Y.D. (2019). Pathological brain detection based on AlexNet and transfer learning. Journal of Computational Science, 30: 41-47. https://doi.org/10.1016/j.jocs.2018.11.008

[21] Fang, T. (2018). A novel computer-aided lung cancer detection method based on transfer learning from GoogLeNet and median intensity projections. In 2018 IEEE International Conference on Computer and Communication Engineering Technology (CCET), Beijing, China, pp. 286-290. https://doi.org/10.1109/CCET.2018.8542189

[22] Mahmood Khan, R.N., Hussain, L., Alluhaidan, A.S., et al. (2025). COVID-19 lung infection detection using deep learning with transfer learning and ResNet101 features extraction and selection. Waves in Random and Complex Media, 35(4): 7886-7909. https://doi.org/10.1080/17455030.2022.2091807

[23] Mannor, S., Peleg, D., Rubinstein, R. (2005). The cross entropy method for classification. In Proceedings of the 22nd International Conference on Machine Learning, Bonn, Germany, pp. 561-568. https://doi.org/10.1145/1102351.1102422

[24] Schofer, M.D., Efe, T., Timmesfeld, N., Kortmann, H.R., Quante, M. (2009). Comparison of kyphoplasty and vertebroplasty in the treatment of fresh vertebral compression fractures. Archives of Orthopaedic and Trauma Surgery, 129(10): 1391-1399. https://doi.org/10.1007/s00402-009-0901-1

[25] Maynard, A.S., Jensen, M.E., Schweickert, P.A., Marx, W.F., Short, J.G., Kallmes, D.F. (2000). Value of bone scan imaging in predicting pain relief from percutaneous vertebroplasty in osteoporotic vertebral fractures. American Journal of Neuroradiology, 21(10): 1807-1812.